Journal of Energy Storage 73 (2023) 108865

Contents lists available at ScienceDirect

Journal of Energy Storage

journal homepage: www.elsevier.com/locate/est

Research papers

Operating performance of a Joule-Brayton pumped thermal energy storage system integrated with a concentrated solar power plant

Mario Cascetta [a], Fabio Licheri [a], Rosa P. Merchán [b], Mario Petrollese [a,*]

[a] Department of Mechanical, Chemical and Materials Engineering, University of Cagliari, Via Marengo, 2, 09123 Cagliari, Italy
[b] Department of Applied Physics and Institute of Fundamental Physics and Mathematics (IUFFYM), University of Salamanca, 37008 Salamanca, Spain

ARTICLE INFO

Keywords:
Energy storage
Concentrated solar power
Pumped thermal energy storage
Packed-bed thermal energy storage

ABSTRACT

The expected performance of an innovative Pumped Thermal Energy Storage (PTES) system based on a closed-loop Brayton-Joule cycle and integrated with a Concentrated Solar Power (CSP) plant are analysed in this study. The integrated PTES–CSP plant includes five machines (two compressors and three turbines), a central receiver tower system, three water coolers and three Thermal Energy Storage (TES) tanks, while argon and granite pebbles are chosen as working fluid and storage media, respectively. A sizing of the main components of the integrated plant has been firstly carried out for the design of an integrated PTES-CSP plant with a nominal net power of 5 MW and a nominal storage capacity of 6 equivalent hours of operation. Specific mathematical models have been developed in MATLAB-Simulink to simulate the PTES and CSP subsystem in different operating conditions, and to evaluate the thermocline profile evolution within the three storage tanks during/charging and discharging processes. A control strategy has finally been developed to determine the operating modes of the plant based on the grid service request, the solar availability, and the TES levels. The performance of the system during a summer and a winter day have been analysed considering the integration of the PTES subsystem in the Italian energy market for arbitrage. Results have demonstrated the technical feasibility of the hybridization of a PTES system with a CSP plant and the ability of the integrated system to participate to energy arbitrage, although a lower exergy roundtrip efficiency (about 54 %) has been observed with respect to the sole PTES system (about 60 %).

1. Introduction

Nowadays, the key medium-term challenge in the electricity sector is to develop technologies able to produce electric energy that would be renewable, efficient, and clean, but, at the same time, ensuring and guaranteeing dispatchability and control of the generation process [1,2]. In this way, the current energy paradigm reveals the importance of feasible, cost-effective, and large-scale energy storage systems for the adequate integration of Renewable Energy Sources (RES) into the energy market [3]. A large variety of energy storage solutions, characterized by different technology readiness level and suitable for specific applications, exists and is being investigated at present [1]. Among these energy storage technologies, the most significant ones, classified by the form of energy stored, are mechanical, electro-chemical, chemical, electrical, and thermal [4]. Some of them rely on toxic materials or have a short lifetime (as the Pb-A batteries), others are very expensive at grid-scale (for instance Li-ion batteries) or restricted by geographical or geological conditions (such as pumped hydro storage and compressed air storage) or achieve low efficiencies (like some chemical systems) [1,4]. There is a common agreement that makes Thermal Energy Storage (TES) one of the ideal candidates for long-term energy storage [5] mainly due to its low capital cost [6]. One of the most straightforward integrations of such storage systems with RES-based generators can be found in Concentrated Solar Power (CSP) plants. TES systems fulfil the requirement of increasing the current solar energy capacity factor for helping CSP technology to be highly dispatchable [7]. Furthermore, the Levelized Cost of Electricity of CSP facilities can be significantly lowered by means of the integration with TES [3,6].

A promising solution for the large-scale storage of electrical energy involving TES is the Pumped Thermal Energy Storage (PTES). In these storage systems, electricity is converted into thermal energy through a heat pump during the charging process and stored in TES reservoirs. A heat engine is then used to convert the stored heat into electrical energy during the discharging process [8,9].

PTES systems are therefore not only free of those abovementioned

* Corresponding author.
E-mail address: mario.petrollese@unica.it (M. Petrollese).

https://doi.org/10.1016/j.est.2023.108865
Received 7 April 2023; Received in revised form 18 August 2023; Accepted 28 August 2023
Available online 18 September 2023

Nomenclature

Symbols

A	area [m^2]
D	diameter [m]
E	energy [kWh]
N	rotational speed [−]
$\dot{Q}$	thermal power [kW]
Q	thermal energy [kWh]
T	temperature [K]
U	overall heat transfer coefficient [W/m^2K]
$\dot{V}$	volumetric flow rate [m^3/s]
$\dot{W}$	electrical power [kW]
c	specific heat [kJ/kg K]
h	specific enthalpy [kJ/kg]
k	thermal conductivity [W/m K]
$\dot{m}$	mass flow rate [kg/s]
p	pressure [Pa]
t	time [h]
α	convective heat transfer coefficient [W/m^2K]
β	compression ratio [−]
γ	heat capacity ratio [−]
ε	void fraction [−]
ϵ	emissivity [−]
η	efficiency [−]
ρ	density [kg/m^3]

Acronyms

CSP	Concentrated Solar Power
DNI	Direct Normal Irradiance
EH	Electric heater
HT	High Temperature
HTF	Heat Transfer Fluid
LT	Low Temperature
MT	Medium Temperature
ORC	Organic Rankine Cycle
PTES	Pumped Thermal Energy Storage
RES	Renewable Energy Source
SM	Solar Multiple
TES	Thermal Energy Storage
WCO	Water Cooler

Subscripts

C	compressor
CD	condenser
EV	evaporator
H	heliostats
P	pump
REC	recuperator
SH	superheating
T	turbine
WF	working fluid
amb	ambient
i	inlet
ins	insulation
is	isentropic
em	electro-mechanical
net	net power
nom	nominal conditions
o	outlet
p	particle
rec	receiver
s	solid medium
set	set point
th	thermal

drawbacks but are expected to store heat at large-scale (MWh) with low costs [10,11], flexible power ratings heat [12], low self-discharge rate, small installation footprint, high life cycle [13], and high scalability [14]. Moreover, PTES features a high energy storage density [15] that makes the use of artificial storage reservoir tanks possible [11] to store energy in the form of sensible and/or latent heat [12]. In this context, large amounts of energy could be potentially stored close to the production areas or to places characterized by high energy demand [15]. Finally, PTES system can also be integrated with external heat sources, which can further increase the ratio between supplied electrical energy during charging and useful electrical energy released during discharging [16].

In the last years, a significant research effort is being devoted to Pumped Thermal Energy Storage because of its advantages [14]. Nevertheless, just few prototypes have been built [14,17] and more research studies regarding fundamental and techno-economic aspects are still required [18]. Referring to the employed thermodynamic cycle, PTES can be mainly classified into layouts that employ Joule-Brayton cycles or Rankine cycles [13,19]. Typically, Rankine-based PTES are involved in low temperature applications and organic fluids are usually preferred as working fluids instead of steam [19]. Although the components of organic Rankine cycles are sufficiently consolidated, the associated thermal efficiencies are still low [19]. PTES systems based on Joule-Brayton cycles are increasing attention [20] thanks to the high efficiencies that can be reached at high temperatures. Indeed, roundtrip efficiencies are not subject to Carnot's limit [20] and roundtrip efficiencies of 100 % could be ideally obtained [21,22]. Nonetheless, system irreversibility decreases the delivered energy [21] and values up to 60 % are usually achieved [12,20]. In this regard, Steinmann et al. tested five different configurations of PTES to assess the irreversibility impact on the system performance and to determine key aspects for the future development of PTES [21]. They found that, for Brayton PTES systems, isentropic efficiencies of turbines and compressors should be around 0.9 to achieve roundtrip efficiencies over 60 %, which allows them to be competitive at large scale [21]. Similarly, Howes et al. estimated a roundtrip efficiency of 72 % for a Brayton PTES system using argon as working fluid and coupled to a packed-bed TES system filled with granite [23]. Usually, gases that are stable at high temperatures, chemically inert, cheap, and environmentally friendly, such as argon, helium, nitrogen and air, are employed as working fluid [24]. Even though there is more experimental background on air turbomachinery, nowadays argon is the preferred option due to the higher temperatures that can be reached respect to the air for the same pressure ratio [17,24]. Furthermore, closed cycles are generally preferred over open ones [19]. Concerning the storage material, sensible media constitute the most adequate option for Brayton PTESs [19]. Thus, packed bed systems made by solid media are the most chosen storage for Brayton PTES thanks to the direct heat transfer between the cycle fluid and the advantages deriving from the use of solid materials (like some gravel or rocks) [17]. The latter are, in fact, cheap, abundant, non-reactive, and have a wide associated temperature interval [25]. Aside these strengths, packed-bed main drawbacks are associated with the need of pressurization, which increments the capital costs, and to the careful management for the thermocline [25]. Therefore, although packed-bed systems have been broadly researched in the last years, the optimal integration of packed-bed TES systems in PTES plants is still an open issue. Packed-beds are usually simulated by means of 1D numerical transient models that include continuity and energy equations, as performed by Esence

et al., who modelled the packed-bed as a continuous porous medium [26]. González-Ayala et al. studied the internal and external irreversibility of a Brayton PTES system with liquid storage media and performed a multi-objective and multi-parametric optimization through the Pareto front [27]. They found that the roundtrip efficiency of the PTES can be risen until 49 % compared to the endoreversible case for maximum power [27]. Zhang et al. carried out a parametric optimization and a thermo-economic performance analysis on PTES systems characterized by charge-discharge cycles at various duration and different TES aspect ratio and storage media [28]. Results demonstrated that important reduction in the levelized cost of storage may arise with the increase of the charging or discharging duration but an optimization in the TES design is required [28].

Since the PTES systems are usually coupled with renewable-based power plants, these storage systems should frequently operate under off-design conditions and the performance evaluation during operation conditions is therefore another important aspect to be investigated. The dynamic characteristic of a 5 MW Brayton PTES system was analysed by Yang et al. highlighting the importance of establishing a proper control strategy to address the input power disturbance and thermal inertia of the system [29]. Xue et al. investigated the transient heat transfer process in the energy storage reservoirs in a 150 kW Brayton PTES based on packed-bed latent heat [30]. Results showed how the operating compression and expansion ratios affect the temperature profiles of the TES reservoirs, the input and output power of the compressor and expander and, thus, the system performance [30].

As mentioned, PTES systems can be easily configured to also absorb heat from external heating/cooling sources. In this regard, the integration between PTES systems and CSP plants is one of the most interesting solutions thanks to the possibility of sharing some components between the two subsystems (such as the power generation unit and the TES system), increasing the operating times of the integrated system and reducing the periods when the power block operates under off-design conditions. Despite the significant potential, only few papers investigated the integration of PTES systems with CSPs [31–35]. Most of them were based on Rankine cycles [31,32,34] and only Frate et al. also investigated the dynamic behavior of such integrated systems [32]. Concerning the integration of Brayton PTES with CSP, McTigue et al. analysed the integration of a supercritical CO_2 PTES system with a CSP plant [33], demonstrating the feasibility of integrating a PTES system with a solar field. Petrollese et al. [35] proposed a direct integration of a Brayton PTES system with a CSP plant including three storage sections. The optimal design in terms of the maximum exergetic roundtrip efficiency of such configuration was found in [35].

Although several potential integration schemes of PTES and CSP can be found in literature, the dynamic of such systems, including both input and output electrical and thermal power fluctuations, is poorly investigated. The aim of the present work is to fill this gap in literature, analysing the ability of the proposed PTES-CSP plant to follow predefined load curves, by considering both the off-design performance and dynamics of the PTES components (TES systems, compressors and expanders, heat exchangers etc.) and the daily fluctuations of solar radiation. This approach aims to demonstrate the actual feasibility of the plant to operate in energy arbitrage, to analyse the time required by the system and the stability of the control system to reach a given power level and keep it by facing off solar radiation fluctuations and variation in the thermocline profiles.

In order to achieve this goal, the PTES-CSP plant configuration sized in [35], will be further explored in the present work. The mathematical modelling developed for simulating the dynamic behavior of each component will be then introduced together with the control strategy proposed for determining the operating mode to be followed by the integrated plant. Finally, the performance of the integrated PTES-CSP plant and its ability to operate under two different weather conditions will be investigated.

2. System design

The system configuration investigated in this study, and already described in [35], is shown in Fig. 1. The two subsystems (the PTES and the CSP) operate with the same working fluid following an inverse or direct Brayton cycle during charging and discharging phases, respectively. The main components of this system are 5 turbomachines (2 compressors and 3 turbines) equipped with dedicated electrical motors driven by inverters or generators, 3 single-tank thermocline packed-bed TES systems operating at different temperature levels, 3 water coolers (WCO) used to cool down the overheating due to machines irreversibility, an auxiliary electric heater and a gas-phase solar receiver where the solar radiation collected by a heliostat field is concentrated.

The system can operate in five operating modes depending on the electrical market and weather conditions. During off-peak periods, usually characterized by low electricity purchasing costs, and without energy solar availability (for instance, during night hours), the system operates under PTES-only charging mode.

In this case, the working fluid is firstly compressed by C1 (12−13), sent to the medium temperature TES (MT-TES) for charging (5–4) and further cooled (15–16) by WCO1. Then, the working fluid expands in turbine T1 (16–17) leading to temperatures usually lower than the ambient one. The working fluid returns to the initial conditions (1−11) through a low temperature TES (LT-TES), where the cryogenic energy is stored. To stabilize the maximum temperature reached by the working fluid to the nominal one, an auxiliary electric heater (EH) is also introduced downstream of the compressor (13–14).

In case of availability of thermal power from the solar receiver during off-peak periods (usually during afternoon), the CSP-PTES operates in charging mode. In these conditions, the CSP is also working, and the thermal energy produced by the solar receiver is stored in a high temperature TES (HT-TES), since the immediate electricity production would not be profitable due to the low selling prices. During this operating mode, the working fluid compressed in C1 is partially or completely sent to the solar receiver (25–26) and the thermal energy produced is stored in the HT-TES (21−20). Then, the working fluid follows the same path as for the PTES-only charging mode, since for the optimal integration between the PTES and CSP subsystems the outlet temperature of the working fluid at the HT-TES (T_{20}) is set equal to that set as the maximum temperature of the MT-TES (T_5).

When the selling prices are high enough, the plant performs the discharging phase. The working fluid is firstly cooled down in the LT-TES (11−1), where it reaches temperatures lower than ambient one, then it is compressed in the C2 (2–3) and heated up in the MT-TES (4–5). In case of solar energy availability and/or HT-TES not completely discharged, the working fluid is sent to the CSP subsystem for a further increase of its temperature up to the maximum one (25–26 and/or 20–21) and, subsequently, sent to the turbine T3 (22−23) and cooled to its initial condition in the WCO3 (23–24). In case the CSP subsystem is not operative, the PTES-only discharging mode is followed, in which the working fluid is heated up in the MT-TES and directly sent to the turbine T2 (8–9), where it expands; then it is cooled by WCO2 (9–10) up to the initial condition.

The CSP-only mode could be also followed in case of solar availability and no activation of the PTES subsystem. In this operating mode, after the compression in the C1 (12–13), the working fluid is heated up by means of the solar receiver and/or the HT-TES (25–26 and/or 20–21) depending on the solar availability and the HT-TES state-of-charge. The working fluid then expands in turbine T3 (22–23) and is further cooled down in the WCO3 (23–24) to its initial conditions. However, the CSP-only mode is rarely used due to the expected low conversion efficiency (<8 %) and the advantages in economic terms of a continuous operation of the PTES subsystem in the energy market.

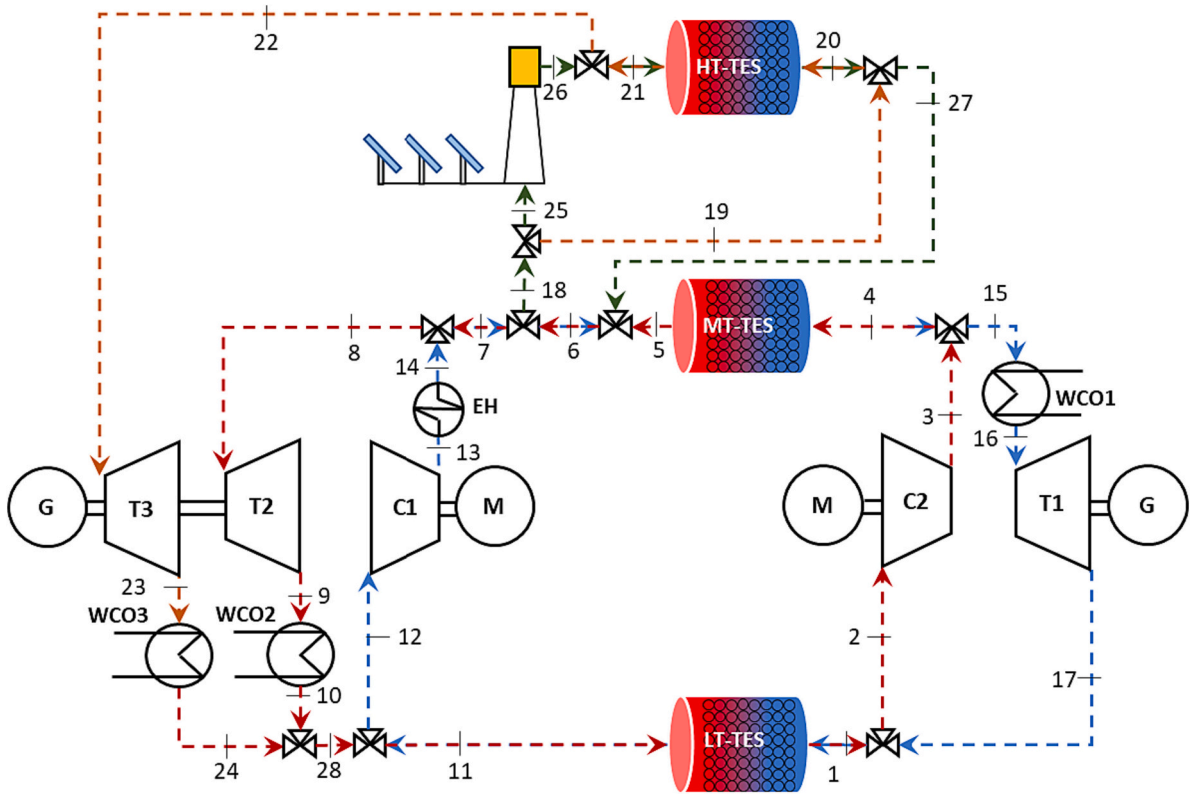

Fig. 1. System configuration of the integrated PTES–CSP plant.

2.1. Thermodynamic cycle

The thermodynamic cycle under nominal condition has been determined based on the parametric analysis conducted in [35] on three design parameters (compressor pressure ratio, WCO1 outlet temperature and WCO2/WCO3 outlet temperature) with the aim of maximizing the exergy roundtrip efficiency of the integrated PTES-CSP. It was assumed the use of argon as working fluid, a minimum cycle pressure of 1 bar and a maximum temperature reached in the solar receiver of 1000 K. To analyse the exergy efficiency and the exergy losses at component level, the typical exergy rate balance equation at steady state was implemented for each component, as follows:

$$\sum \dot{m}_i e_i + \dot{Q}\left(1 - \frac{T_{amb}}{T_c}\right) = \sum \dot{m}_o e_o + \dot{W} + \dot{E}x_D \quad (1)$$

where $\dot{m}$ is the mass flow rate of the stream substance, $\dot{Q}$ is heat flow through component boundary, T_{amb} is the ambient temperature, T_c is the temperature at component boundary, at which heat is exchanged with the environment, e is the specific exergy of the stream (based on the system configuration only the physical exergy defines the total specific exergy of such streams), $\dot{W}$ is work rate of the component, and $\dot{E}x_D$ is the exergy destruction in the component due to irreversibility. The nominal

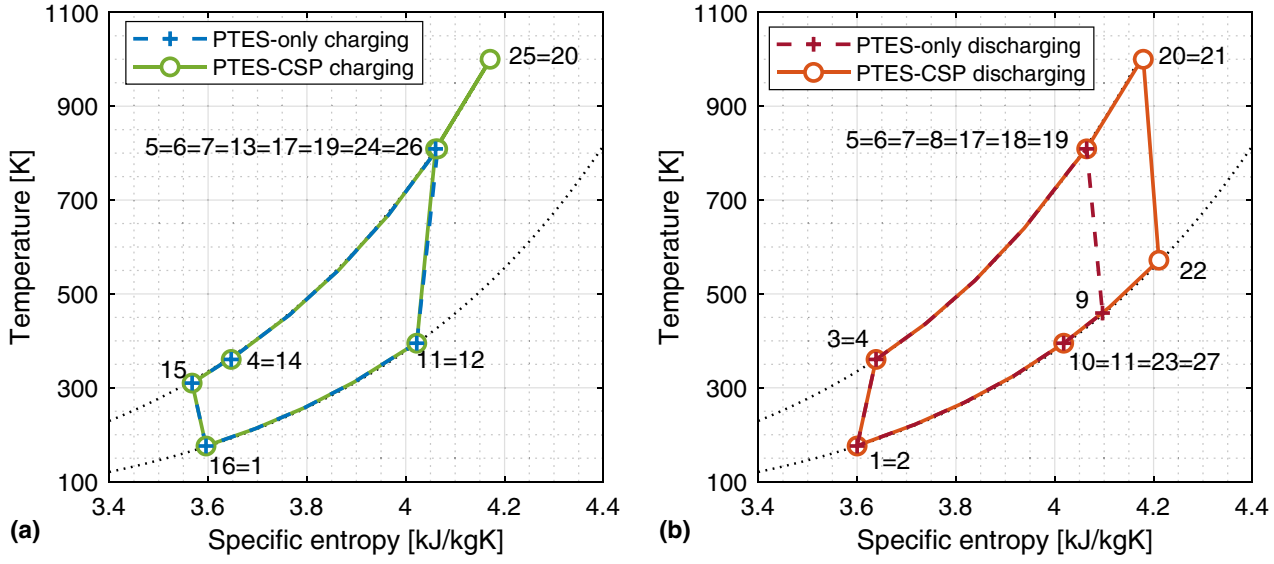

Fig. 2. Thermodynamic cycles during (a) charging phases and (b) discharging phases.

exergetic roundtrip efficiency of the overall system, defined as the ratio of the electrical energy delivered during a complete discharging phase to the electrical energy absorbed and the exergy input in the solar receiver during a fully charging phase, was then computed. The maximum exergetic roundtrip efficiency (i.e., a value of 58.2 %) was reached by a Brayton cycle characterized by a compressor pressure ratio of 5.2, with a WCO1 outlet temperature of 310 K and a WCO2/WCO3 outlet temperature of 395 K. Fig. 2 shows the thermodynamic cycles followed during the various plant operating modes. The desired thermodynamic conditions have been used in this study for sizing the main components, as explained in the following. The integrated PTES-CSP plant has been designed to produce a nominal net power during the discharge phase of 5 MW with a nominal storage capacity of 6 equivalent hours of operation.

2.2. Turbomachinery design

The peculiarities of the proposed plant (low temperatures and argon as working fluid) demand a specific design of the compressors to be used. The expected operating conditions have led to the selection of two multistage centrifugal compressors, due to their reduced specific speed, both made of 4 stages. In order to predict the design and off-design performance of the compressors, the Casey-Robinson method [36] has been used. The method ensures a good accuracy in performance prediction [37] despite the reduced number of parameters required at the design point and a little knowledge of geometric characteristics. Thanks to the non-dimensional parameter formulation, the correlations can be used not-only for air but also for other gases, which makes the method of general validity. The prediction method has been implemented by introducing a stage-stacking approach to build the overall characteristic of each compressor. The compressor polytropic peak-efficiency has been assumed equal to 0.86, considering a tip-speed Mach number of 0.8 as follows from the correlations proposed in [38]. Vaneless diffusers have been considered, as typically done in designing process compressors [36,37].

2.3. Thermal energy storage design

Since the three packed-bed TES systems operate at different temperature levels, a proper design for each tank has been required. Granite pebbles have been selected as solid storage media thanks to the wide temperature range they can operate at and for their low price. Based on the desired storage capacity, here expressed in equivalent hours of operation (Δt_{TES}), the stored energy (E_{TES}) of a given TES can be calculated as follows:

$$E_{TES} = \dot{m}_{WF}\bar{c}_{WF}\left(T_{WF,i} - T_{WF,o}\right)\cdot\Delta t_{TES} \tag{2}$$

where $\dot{m}_{WF}$ and $\bar{c}_{WF}$ are the mass flow rate and average specific heat of the working fluid respectively, while $T_{WF,o}$ and $T_{WF,i}$ are the outlet and inlet fluid temperatures at design conditions, respectively. The size of the TES system suitable for storing the requested amount of energy has been found through a preliminary numerical simulation. The sizing has been carried out considering that a complete exploitation of the TES device is not possible due to the constraints imposed by the turbomachines that can accept only a limited deviation of the inlet gas temperature from the nominal conditions. Indeed, a great deviation would lead the turbomachines, in particular the compressors, to operate under significant off-design conditions resulting in reduced system efficiencies. On the other hand, a strict limit imposed on the terminal temperatures would generate a hysteresis phenomenon inside the packed-bed with a consequent degradation of the thermocline and a decrease in storable thermal energy with the progression of the cycles. Based on preliminary numerical simulations, a threshold value of 25 K in outlet temperatures with respect to the design conditions to all the TES systems has been set. The only exception is the threshold value imposed to the bottom of the LT-TES that is reduced to 5 K, since the numerical simulations showed that it heavily affects the compressor performance during the discharging phase. These preliminary simulations were made running five consecutive charge/discharge cycles to exclude the generation of the hysteresis phenomenon and to have the TES systems already at a regime condition. Table 1 reports the size of the three storage tanks, by assuming an aspect ratio of 3. These values are inversely proportional to the operative temperature range while the specific heat of the granite is increasing with the temperature. Consequently, the combination of these two factors leads to a larger size for the LT-TES compared to HT-TES and MT-TES. Another effect to be accounted is the hysteresis that is more emphasized when the temperature range is high, leading therefore to a greater size.

2.4. Solar central receiver design

Among the CSP technologies available at medium-large power scale, a central receiver tower system has been chosen for the high temperatures this solar plant can reach, which perfectly match with those usually obtained in Brayton PTES systems [39,40]. A polar heliostat field has therefore been selected for concentrating solar radiation into a pressurized volumetric receiver [41]. Assuming that, as predicted by Kusterer et al., the difference between the ceramic foam temperature and the gas temperature at the outlet of the receiver is at the same level for air and argon [41], argon is the fluid heated up in the absorber, as it has also been supposed in [42,43].

For the design of the heliostat field, meteorological data, such as Direct Normal Irradiance (*DNI*) and ambient temperature (T_{amb}), observed on 11th of July (193rd day of the year) at 12 h in Cagliari (Italy, latitude 39.23° N and longitude 9.12° E) during clear sky conditions have been considered. For the evaluation of the optical efficiency of the heliostat field (η_0), the cosine ($cos\omega$), the spillage (f_{sp}), the attenuation (f_{at}), the blocking (f_b), and the shadowing (f_{sh}) effects together with the actual mirror reflectivity (λ) have been considered for each individual heliostat. Then, the average efficiency has been calculated considering the number of heliostats (n_H) [44,45]:

$$\eta_0 = \frac{\sum_{h=1}^{n_H}\eta_{H_h}}{n_H} = \frac{\sum_{h=1}^{n_H}\left[cos\omega_h \cdot f_{sp_h} \cdot f_{at_h} \cdot f_b \cdot f_{sh} \cdot \lambda\right]}{n_H} \tag{3}$$

By assuming a solar multiple (*SM*) of 1.2, a heliostat field of 56 square heliostats, each of them with an area (A_H) of 120 m^2, subdivided in 7 rows in a 90° angle polar field, has been therefore chosen for collecting the solar radiation required to generate the design thermal power in the solar receiver. The latter has been modelled as a lying cylinder in which the circular base has two diameters: the outer diameter, relating to the total volume of the receiver where the heat absorption happens; and the inner one ($D_{rec,in}$), which corresponds to the aperture diameter in the tower and is used for the calculation of the aperture surface of the receiver, is smaller than the first one to minimize conduction losses (even though this increases spillage).

The concentration factor, defined as the ratio of the aperture area of the heliostat field (A_a) to the receiver area (A_{rec}):

$$C = \frac{A_a}{A_{rec}} = \frac{n_H{}^* A_H}{\pi^*\left(\frac{D_{rec,in}}{2}\right)^2} \tag{4}$$

Table 1
Sizing of the three TES systems.

Storage system	LT-TES	MT-TES	HT-TES
Temperature difference [K]	224	467	177
TES volume (V_{TES}) [m^3]	994	883	452
Diameter [m]	15.6	15.0	12.0
Height [m]	5.2	5.0	4.0

has been finally calculated for this solar receiver tower, achieving a value of 1131. The main design parameters of the tower system are summarized in Table 2.

2.5. Water coolers

Three water coolers are introduced in the system to deal with the extra heating due to the irreversibility produced in the compressors and turbines. The water coolers have been designed by considering an inlet water temperature of 298 K and a temperature increase of 25 K under design conditions (the temperature levels of the working fluid were already determined by defining the thermodynamic cycle). TEMA shell-&-tube heat exchangers characterized by one shell pass and two tube passes (the working fluid flows inside the tubes to minimize pressure losses) with a triangular mesh characterized by a tube pitch ratio of 1.3 have been chosen according to the operating conditions. The single tube has been characterized by a length of 5 m, an inner diameter of 41 mm and a thickness of 3.5 mm. By assuming an overall heat exchange coefficient of 200 W/m^{2}K, the requested heat exchange area has therefore been determined, together with the design effectiveness and the main geometric features of the heat exchanger. Table 3 reports the main design characteristics of the three water coolers.

3. Mathematical model

Starting from the sizing of the main components, a mathematical model for assessing the performance of the integrated PTES–CSP plant during different operating conditions has been developed in MATLAB-Simulink, while the Coolprop database [46,47] has been used for the evaluation of working fluid properties. An implicit Runge-Kutta numerical scheme has been used as differential equations solver, by imposing a maximum time step of 10 s. The main correlations used to simulate the principal components of the proposed plant are introduced in the following together with the control strategy adopted for determining the operating mode.

3.1. Turbomachinery

The operating performance of compressors are based on the coupling between the compressor map and the circuit conditions. Starting from the operating pressures in the LT-and MT-TES, the compression ratio (β_C) has been established and used as main input together with the compressor rotational speed (n_C) to determine the mass flow rate elaborated by the compressor ($\dot{m}_C$) and the corresponding isentropic efficiency (η_C) according to compressor characteristic curves determined during the design phase.

The outlet temperature has been therefore calculated as follows:

$$T_{C,O} = T_{C,I} \cdot \left[\frac{\beta_C^{\frac{\gamma-1}{\gamma}} - 1}{\eta_C} + 1 \right] \quad (5)$$

Table 2
Sizing of the solar central receiver system.

Parameter	Value	Parameter	Value
Receiver length	6 m	Temperature out of the receiver	1000 K
Internal diameter of the receiver	2.75 m	External diameter of the receiver	4.2 m
Heliostats height	10.95 m	Heliostats area	120 m^2
Heliostats number	56	Concentration factor	1131
Actual mirror reflectivity	0.836	Blocking & shadowing factor	0.95
Separation distance between adjacent heliostats	3.3 m	Minimum radius of the heliostat field	65 m
Tower height	65 m	Solar Multiple	1.2

Table 3
Sizing of the three water coolers.

	WCO1	WCO2	WCO3
Logarithmic mean temperature difference [K]	20.9	20.8	153.5
Heat exchange area [m^2]	212.4	269.7	98.8
Effectiveness of the heat exchanger [−]	0.8	0.6	0.4
Shell diameter [m]	1.22	2.18	2.06
Number of tubes [−]	280	900	800

The compressor rotational speed has been regulated by means of an inverter driven by a PI controller, which uses the difference between the desired net power and the actual net power produced by the integrated system as feedback signal. The use of an inverter allows to vary the compressor rotational speed from 70 % to 110 % of its nominal speed. The turbine has been considered to operate under chocking conditions, thus the reduced flow rate is locked. Furthermore, no inverter has been introduced to control turbine's rotational speed, and the mass flow rate elaborated by the turbine ($\dot{m}_T$) can be calculated as a function of the expansion rate and the inlet temperature.

3.2. Thermal energy storage

The thermal behavior of the three TES systems has been evaluated using a transient 1-D two-equation model, by assuming the packed-bed as isotropic, homogeneous, and keeping constant the temperature profile along the radius of the bed. The spatial step of discretization has been set equal to 0.05 m, while the temperature profiles along the axis of the bed have been calculated separately for the working fluid (T_{WF}) and the solid medium (T_S) by means of the following equations:

$$\varepsilon \rho_{WF} c_{WF} \frac{\partial T_{WF}}{\partial t} + \rho_{WF} c_{WF} u \frac{\partial T_{WF}}{\partial z} = \alpha_c A_S (T_S - T_{WF}) - U_{TES} A_{TES} (\overline{T}_{WF} - T_{AMB}) \quad (6)$$

$$(1-\varepsilon) \rho_S c_S \frac{\partial T_S}{\partial t} = k_{eff} \frac{\partial^2 T_S}{\partial z^2} + \alpha_c A_S (T_{WF} - T_{BED}) \quad (7)$$

where k_{eff} is the effective thermal conductivity that also takes into account the radiation contribution within the bed [48], U_{TES} is the overall heat transfer coefficient between the tank and the environment (set to 0.3 W/m^{2}K), A_{TES} is the surface area per unit of volume of the vessel, T_{AMB} is the ambient temperature, ε is the void fraction (assumed equal to 0.4 for all the beds), ρ_S is the density of the granite pebbles (assumed constant and equal to 2690 kg/m^3), while c_S and k_s are the specific heat and thermal conductivity, respectively, calculated by means of two empirical correlations according to experimental tests reported in literature [49,50]:

$$c_S = 5.944 \cdot 10^{-7} \cdot T_S^3 - 2.0197 \cdot 10^{-3} \cdot T_S^2 + 2.387 \cdot T_S + 224 \quad (8)$$

$$k_s = -1.431 \cdot 10^{-3} \cdot T_S + 2.952 \quad (9)$$

The convective heat transfer coefficient α has been correlated to the Nusselt number calculated according to a well-known empirical correlation reported in Eq. (10) [51,52], while the surface area per unit of volume of the bed A_S depends on the particle diameter (d_p) and void fraction (ε) as reported in Eq. (11):

$$Nu = 2.0 + 1.1 \cdot Re_p^{0.6} \cdot Pr^{0.33} \quad (10)$$

$$A_S = \frac{6 \cdot (1-\varepsilon)}{d_p} \quad (11)$$

The effective thermal conductivity of the bed k_{eff} depends mainly on the conductivity of both the solid (k_S) and the fluid (k_{WF}) (Eq. (12)). The correlation also includes the effects of thermal radiation, not negligible at temperatures higher than 300 °C [53]:

$$k_{eff} = k_{WF}\left[\varepsilon\left(1+\tau\frac{\alpha_{rv}d_p}{k_{WF}}\right)+\frac{\tau(1-\varepsilon)}{\frac{1}{\phi+\frac{\alpha_{rs}d_p}{k_{WF}}}+\frac{\theta}{\frac{k_S}{k_{WF}}}}\right] \quad (12)$$

where τ represents the ratio between the distance of the centres of two adjacent solid pebbles and the diameter of the pebble (set to 0.9), θ is the ratio of the pebble length to the diameter of the pebble (assumed equal to 2/3), the factor ϕ measures the thickness of the fluid film adjacent to the contact point of two solid pebbles [48,53], while, α_{rv} and α_{rs} are the void-to-void and solid-to-solid surface radiative heat transfer coefficients, which are calculated according to the following equations:

$$\alpha_{rv} = \left[\frac{0.1952}{\left(1+\frac{\varepsilon}{2(1-\varepsilon)}\frac{1-\epsilon_s}{\epsilon_s}\right)}\right]\left(\frac{T_{WF}}{100}\right)^3 \quad (13)$$

$$\alpha_{rs} = 0.1952\left(\frac{\epsilon_s}{2-\epsilon_s}\right)\left(\frac{T_S}{100}\right)^3 \quad (14)$$

Both these correlations depend on ϵ_s that is the solid emissivity, which has been set to 0.85.

With regards to the operative pressure of the vessel, the variation over time of the average pressure inside the tank has been calculated by applying the mass conservation equation for compressible flows:

$$\frac{\varepsilon V_{TES}}{\gamma R\overline{T}_{WF}}\frac{dp}{dt} = \dot{m}_i - \dot{m}_o \quad (15)$$

where γ is the heat capacity ratio, R is the specific gas constant, $\dot{m}_i$ and $\dot{m}_o$ are the inlet and outlet mass flow rates respectively. In addition, the pressure losses inside the packed-bed are evaluated according to the well-known Ergun equation:

$$\frac{\nabla p}{L} = 150\cdot\mu\cdot\frac{(1-\varepsilon)^2}{\varepsilon^3 d_p^2}\cdot v + 1.75\cdot\frac{(1-\varepsilon)}{\varepsilon^2 d_p}\cdot\rho\cdot v^2 \quad (16)$$

3.3. Solar central receiver

The solar thermal power delivered by the receiver ($\dot{Q}_{rec}$) to the HT-TES, which mainly depends on DNI and ambient temperature, has been computed as the heliostat field power subtracting thermal losses regarding conduction, convection, and radiation in the receiver [44,45]:

$$\dot{Q}_{rec} = \eta_0\cdot DNI\cdot A_a - A_r\left[\epsilon_{rec}\cdot\sigma\cdot\left(T_{rec}{}^4 - T_{amb}{}^4\right) + U_{rec}\cdot\left(T_{rec}-T_{amb}\right)\right] \quad (17)$$

where T_{rec} is the receiver temperature and σ is the Stefan-Boltzmann constant. ϵ_{rec} represents the effective emissivity of the receiver surface, assumed equal to 0.1, and U_{rec} corresponds to the overall conduction and convection heat transfer coefficient, considered for this system equal to 5 W/(m^{2}K).

Since the HT-TES needs a constant inlet temperature, the temperature at the outlet of the receiver must be around 1000 K, although solar conditions vary with time, and the mass flow at the solar receiver should be regulated to keep the receiver outlet temperature as constant as possible. Therefore, the mass flow rate at the outlet of the receiver ($\dot{m}_{rec}$) has been calculated as:

$$\dot{m}_{rec} = \frac{\dot{Q}_{rec}}{\left(h_{o,rec}-h_{i,rec}\right)} \quad (18)$$

where $h_{o,rec}$ is the specific enthalpy at the outlet side of the solar receiver corresponding to a temperature of 1000 K while $h_{i,rec}$ is the specific enthalpy inlet side of the receiver. An upper limit of 120 % of the design mass flow has been fixed. If higher values are achieved, some heliostats are defocused [54–56]. On the other hand, when the DNI is low, (for instance, during sunrise or during sunset), only a limited mass flow rate could be heated up to 1000 K, introducing problems in the temperature control and increasing the impact of parasitic losses. Therefore, a minimum receiver power equal to the 10 % of the designed one has been set.

3.4. Water coolers

The operating performance of the three working coolers has been simulated by considering a constant effectiveness of heat exchanger. Based on the mass flow rate and temperature of the working fluid at the inlet side of each water cooler, the theoretical maximum heat exchanged has been calculated and, consequently, the exchanged heat (the effectiveness is known) and the actual outlet temperature of the working fluid.

According to [57], the pressure losses at the gas side (Δp_{WC}) have been calculated based on the following correlation:

$$\Delta p_{WC} = \left(4f\frac{LN_P}{d_{in}} + 4N_P\right)\frac{\rho v^2}{2} \quad (19)$$

where f is the friction factor, N_P is the number of tube passes, L and d_{in} are the length and inner diameter of the tube respectively, ρ and v are the density and average speed of the working fluid respectively.

3.5. Operating strategy

The control strategy proposed for the determination of the operating mode, which mainly depends on grid service request, solar availability and TES state-of-charge, is shown in Fig. 3. Firstly, the determination of the charging or discharging phases is defined by the net power requested. The latter mainly depends on the considered application, such as if the PTES-CSP system is devoted to cover a specific load demand or if it offers services to grid. However, the actual activation of the PTES subsystem also requires the monitoring of the state-of-charge of the MT-TES and LT-TES. This is measured by introducing some threshold values in the working fluid outlet temperatures from the considered TES systems, as discussed in Section 2.3. In case the latter constraints are not satisfied, the PTES subsystem is not activated while the CSP subsystem is activated in CSP-only mode if the electrical user required power and the expected thermal power produced by the solar receiver exceeds the 80 % of the nominal one, otherwise all the integrated system is set in idle mode. Therefore, the CSP subsystem is generally activated simultaneously with the PTES subsystem. Specifically, during charging phase the CSP subsystem is activated (and the integrated system operates in PTES-CSP charging mode) if the solar receiver produces a thermal power greater than the 10 % of the nominal receiver thermal power and the HT-TES is not fully charged (like the other tank, this occurs when the outlet temperature exceeds an imposed threshold value), otherwise the system would operate under PTES-only charging mode.

Instead, the activation of the CSP subsystem only depends on the HT-TES state-of-charge during the discharging phase: until the HT-TES can guarantee an outlet temperature higher than an imposed threshold value, the system will operate in PTES-CSP discharging mode; otherwise, only the PTES subsystem will be activated (PTES-only discharging mode). It is worth noting that the integration of the two systems introduces constraints in the operation of the plant especially for the CSP subsystem, which is often forced to postpone the electrical production based on PTES conditions. The proposed operating strategy therefore differs from those usually proposed in literatures for solar tower power plants (such as [58,59]) mainly based on the maximization of the thermal power production and profits from the sale of electricity.

4. Results and discussion

The expected performance of the proposed PTES-CSP plant in

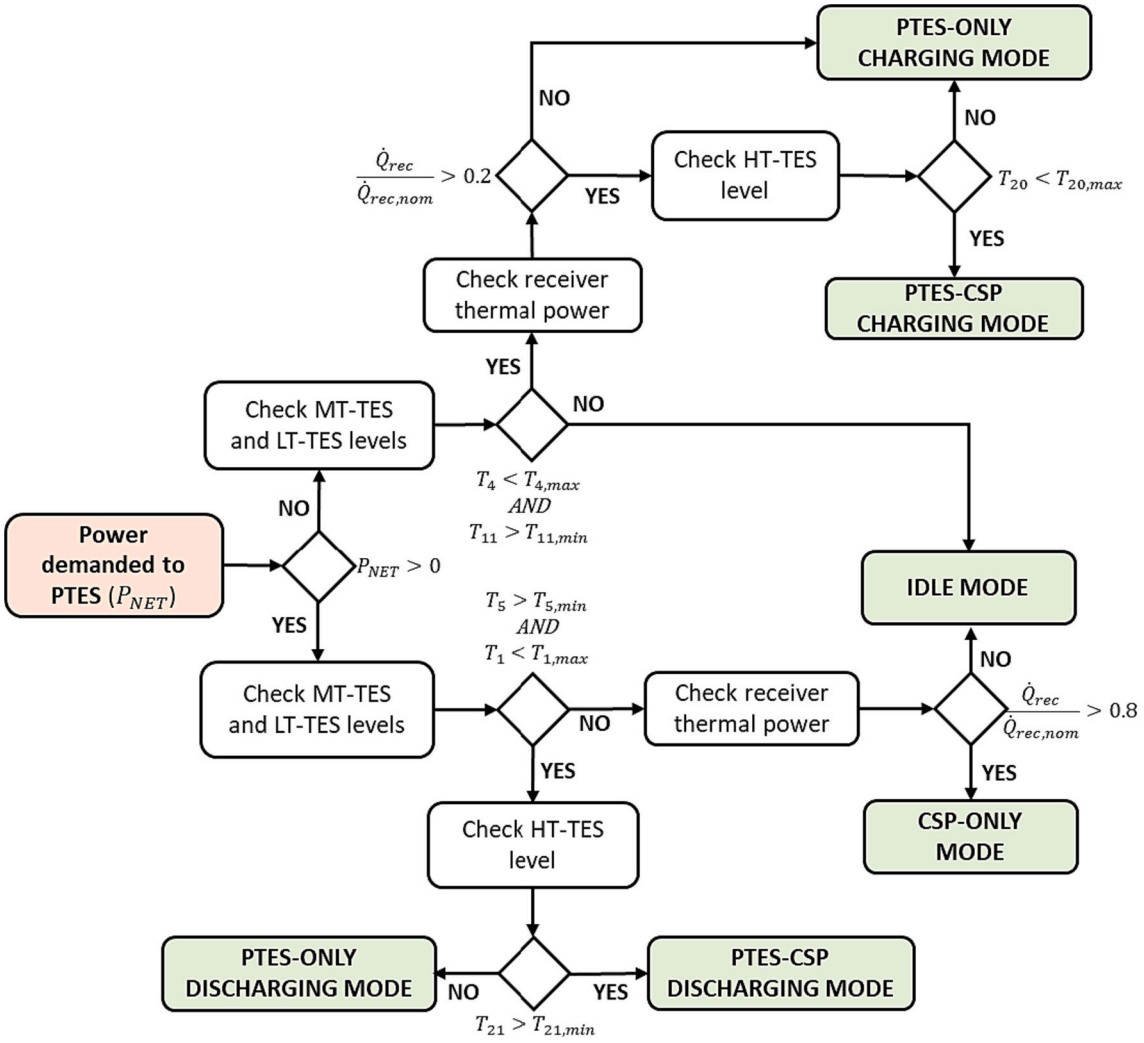

Fig. 3. Operating strategy for the management of the integrated PTES-CSP plant.

different operating conditions are discussed in this section. Two different weather conditions, represented by two profiles of the available DNI, have been investigated to verify the effects on the performance of the integrated PTES-CSP plant. The Case A is representative of a summer day (the 193rd day of the year) with clear sky conditions, while the Case B is a cloudy winter day (the 1st day of the year) in a site located in the Southern Italy (specifically in Cagliari with an expected direct normal irradiation of about 1700 kWh/m^{2}y). Fig. 4 shows the trend of the DNI imposed as main input to evaluate the potential thermal power produced in the solar receiver for both cases. The maximum thermal power that this receiver can deliver for the simulated days is 4 MW$_{th}$. Regarding the PTES subsystem, it is assumed that the storage system is

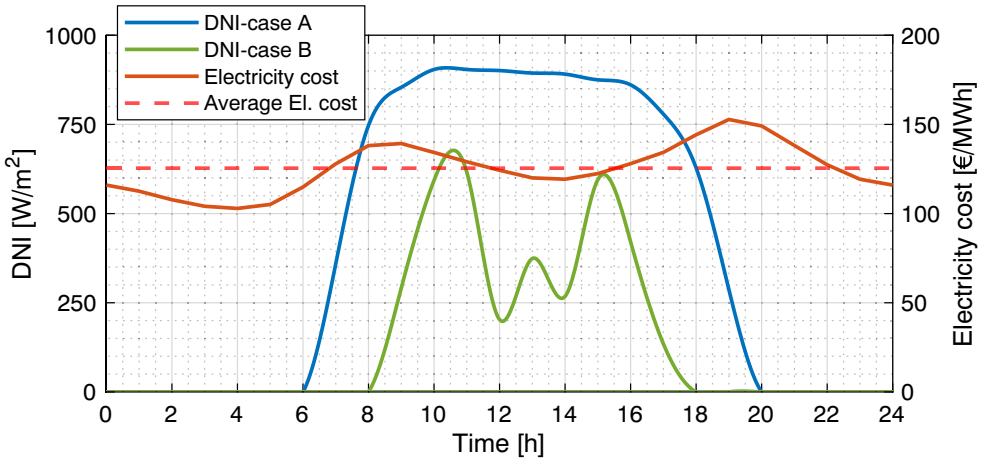

Fig. 4. Direct normal irradiance and electricity cost assumed for the considered case studies.

used for energy arbitrage, taking the yearly-based average hourly electricity cost of the Italian energy market in the 2021 as reference (the electricity cost curve is shown in Fig. 4). When the electricity cost exceeds the daily average cost (about 125 €/MWh for the case study) the PTES is set in discharge mode for producing, if possible, a power equal to the nominal one, while, in the remaining time, the PTES operates in charging mode absorbing the demanded power from the grid.

4.1. Case A

Based on the operating strategy proposed in the previous section, the net power demanded and produced by the PTES-CSP plant during the considered summer day are shown in Fig. 5. As can be observed, the PTES-only charging mode is followed during nighttime due to the low electricity cost. The plant switches to discharging mode during the peak hours in the morning, for about 5 h. During this period, the PTES subsystem is used for energy production, due the low charge of the HT-TES. Then, the electricity cost is lower than the average one and it is convenient to purchase energy from the grid for charging the MT-TES and LT-TES.

The solar plant is also active during this charging phase, and the thermal energy produced in the solar receiver is stored in the HT-TES (PTES-CSP charging mode). The thermal energy stored in the three tanks is used to sell electricity to the grid during the peak hours of the evening and the plant operates in the PTES-CSP discharging mode, thanks to the high state-of-charge of the HT-TES. After that, the charging mode with the activation of the sole PTES subsystem is again selected. The comparison between the requested power and the actual power produced/absorbed by the system is also shown in the same Fig. 5. The results demonstrated a good ability of the controller of the compressors rotational speed to follow the fixed set-point despite the variation of the operating conditions of the machines during the day. A focus on the behavior of turbomachines and TESs during a day is shown in Fig. 6, where power, mass flow rate and pressure levels are reported as a function of time.

The net power of the plant is kept constant during the day-period controlling the rotational speed of the compressor with a consequent variation in the circulating mass flow rate (Fig. 6(b)). The main cause of such variation is the change in gas temperature at the inlet section of the compressors and turbines, leading to a variation in the specific work as well as in the power absorbed by the compressors and produced by the turbines. Fig. 6 shows that the variations in the operating conditions occur especially in the periods preceding a mode change. In the same figure, it is depicted the relative rotational speed of the compressor, that ranges from the 98 % to 110 % of the nominal rotational speed, observed at the end of the second discharged phase (Fig. 6(a)), which partially compensates for the reduction in the specific work caused by the temperature.

Furthermore, the mass flow rate circulating in the solar receiver depends both on the available DNI and on the PTES operation, as shown in Fig. 6(b). During the first discharging phase, the mass flow rate increases gradually, according to the DNI profile, up to a maximum value of about 38 kg/s at the end of the phase. During the subsequent charging phase, the mass flow rate circulating in the receiver is bounded by the mass flow rate required by the PTES subsystem to absorb the desired power from the grid. Consequently, a constant outlet temperature from the receiver cannot be assured and the gas temperature slightly exceeds the designed value reaching a maximum temperature of 1005 K. During the first part of the second discharge phase, all the mass flow rate circulating in the solar receiver is sent to the turbine T3 up to the 17th hour, when the decrease in the solar availability results in a reduction of the receiver mass flow rate and the discharge of the HT-TES. As mentioned, deviations in the machine operating conditions are due to inlet temperature variations, which depend on the thermocline behavior inside the TES. Therefore, it is important to investigate the evolution of the temperature field inside the three tanks. The thermocline profiles calculated during the first charging/discharging cycle with a time interval of 1 h are shown in Fig. 7. As already mentioned, the starting temperature profiles are the results of five complete charging-discharging cycles. This is shown in Fig. 7(a), where the LT-TES initial charged condition corresponds to (0 h) profile. The cold gas enters from the bottom of the tank at about 171 K after expansion in turbine T1 and absorbs heat from the solid media and exits from the top at 395 K. As the charging phase proceeds, the outlet temperature decreases until about 330 K, which means the LT-TES reaches the fully state after 6 h, leading to a change in the operating conditions of the compressor C1, as observed in Fig. 6. Concerning the MT-TES, the hot gas at about 823 K enters the tank and releases its thermal energy content to the solid media. It initially leaves the tank at 356 K but, over time, the thermocline shifts to the right as visible in Fig. 7(c) and the outlet temperature of the gas increases until reaching about 390 K at the end of the cycle after 6 h, confirming a good balance between the design of the two TES involved in the PTES subsystem. Obviously, the thermocline profile of the HT-TES does not change during the first charging phase, see Fig. 7 (e), due to not availability of solar power. After 6 h, the plant switches to the PTES only discharging mode, and the gas flow is reversed inside the three TES systems. Fig. 7(b) clearly shows that the gas inlet temperature is not constant, but slightly increases during the first 2 h while decreases in the last part of the phase. An inverse behavior is observed in the MT-TES, as shown in Fig. 7(d). This is due to the linked effects caused by the introduction of threshold values in the various TESs that modify the operating point - and, therefore, the outlet temperatures - of the machines. Thus, the definition of proper threshold values is of fundamental importance for the good management of the proposed system, which

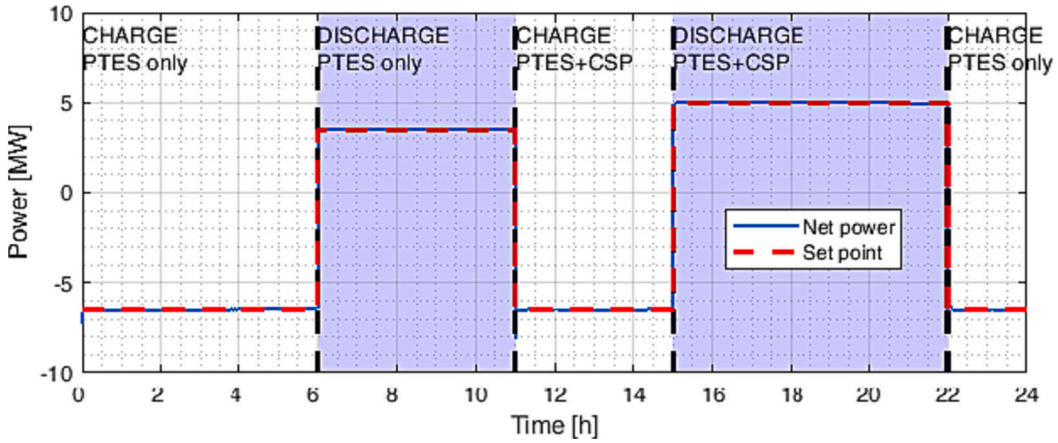

Fig. 5. Net power desired and produced by the PTES-CSP plant for the Case A.

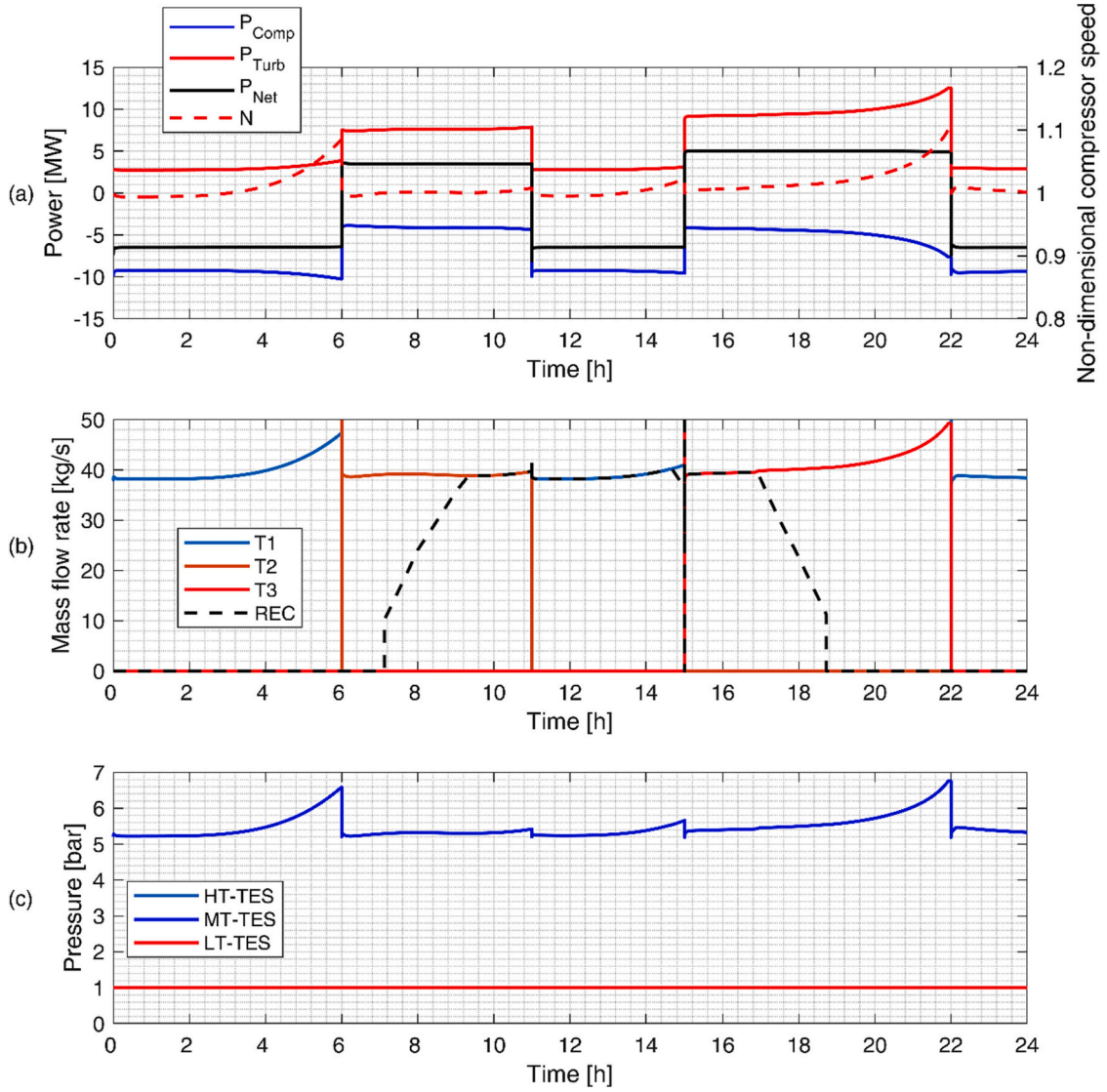

Fig. 6. (a) Compressor and turbine power curves, compressor rotational speed, (b) mass flow rates circulating in the turbines and solar receiver and (c) average TES operating pressures obtained for the Case A.

should be taken as the best compromise between the necessity to avoid the hysteresis effect that usually occurs within the bed after several working cycles and the constraints imposed by the overall system in which the TES systems are integrated. Finally, the evolution of HT-TES temperature profile (Fig. 7(f)) follows a different trend since it is in charging phase, but, due to the low solar availability in the early morning, the fully charge state is not yet reached after 5 h.

The second cycle is clearly a consequence of the first one with the MT-TES and LT-TES that repeat the same behavior already observed during the previous charging-discharging cycle as depicted in Fig. 8 (a–d). The charging phase, which lasts 4 h, is followed by a discharge one with a duration of 7 h. During this last phase, the outlet temperature of the LT-TES reaches a value of about 200 K, while at the exit of the MT-TES the temperature drops to about 800 K, well beyond the threshold imposed at the beginning, but without any issue in the operability of the system. The HT-TES has a completely different behavior since it is strictly related to the availability of the solar DNI and the PTES operation.

During the charging phase of the HT-TES (Fig. 8(e)), the constant mass flow rate circulating in the solar receiver and simultaneous variation in the outlet gas temperature result in temperature fluctuations in the upper part of the thermocline. As mentioned, the HT-TES is fully charged after 4 h. During the discharge phase, the mass flow rate that flows in the HT-TES system is not constant, since it compensates for the thermal power produced in the solar receiver. For this reason, the thermocline profile does not change during the first 2 h before the actual discharging of the TES system occurs. During the discharging phase, the gas temperature sent to the turbine T3 is slightly higher than the designed temperature (1000 K) with a consequent deviation of the T3 operating conditions from the nominal one. Furthermore, since the inlet gas temperature of the HT-TES system moves accordingly to the outlet gas temperature of the MT-TES system, the temperature of the working fluid introduced into the HT-TES drops to 800 K when the complete discharge of MT-TES is reached. At the end of the discharging phase the maximum temperature of the HT-TES is far from the threshold value set equal to 975 K for determining the total discharge of this tank and the residual charging can be exploited during the following day.

4.2. Case B

To demonstrate the ability of the plant to follow predetermined production profiles in different weather conditions, the DNI profile representative of a winter day has been considered. The electricity cost has been assumed equal to the Case A, as well as the control strategy. In

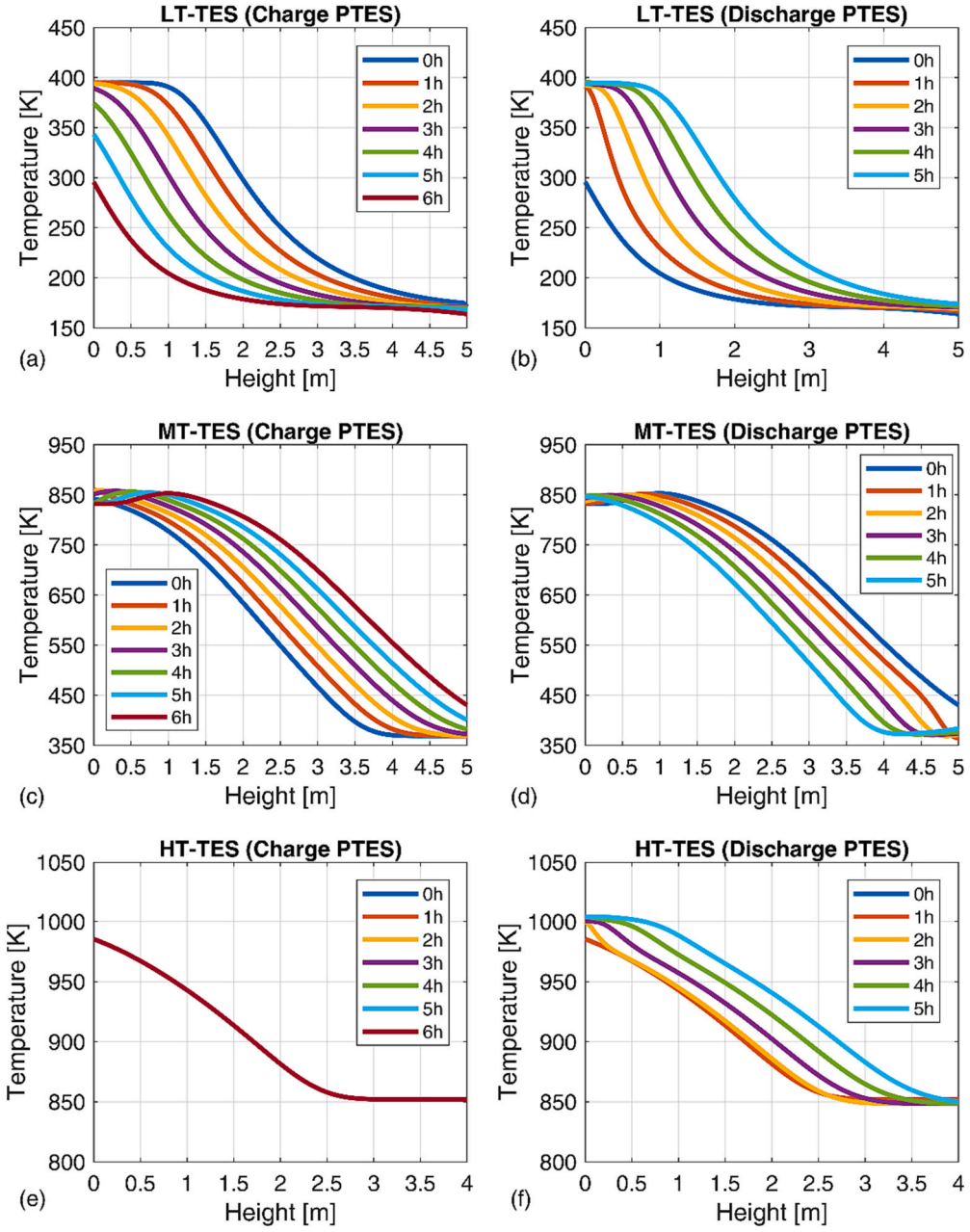

Fig. 7. Thermocline profile evolution in the three TES system during the first charging-discharging cycle for the Case A.

Fig. 9, the net power consumed and produced during the considered winter day is shown. As can be observed, the main variation in the production profile compared to the Case A occurs during the second discharge phase. Due to the lower value of the DNI, the turbine T3 can be kept in operation only for 5 h, until the HT-TES is completely discharged. Subsequently the control system switches to the PTES-only discharging mode, with the activation of the turbine T2 until the end of the discharge phase. However, a drop in the net power produced, and a consequent increased deviation from the set-point, can be observed in this phase.

This is due to the constraint imposed to the compressor speed, which cannot exceed the 110 % of its nominal value. As shown in Fig. 10(a), the compressor speed rapidly increases at the end of this discharging phase until reaching its maximum value, preventing the control system from following the scheduled net power. These conditions mainly depend on the increasing temperature calculated at the inlet section of the compressor, that modifies the operative condition of the machine resulting in a decrease of its performance. Since the power produced by the turbine T2 remains almost constant, the specific work of the cycle tends to decrease and can not be contrasted by the increase in the mass flow rate since the maximum limits have already been reached. This is confirmed by Fig. 10(b), in which the trend of the mass flow rates calculated in the three turbines and within the receiver are shown.

The effect of the constraint of the speed compressor is quite clear with a sharply stop in the increase of the mass flow rate at the end of the second discharge phase close to 50 kg/s. Finally, the different trend in the mass flow rate circulating in the receiver compared to the Case A is highlighted in the same figure.

4.3. *Overall performance analysis*

By considering the two complete charging/discharging cycles, roundtrip efficiencies, defined as the ratio of the electric energy produced during the two discharging phases to the electric energy absorbed

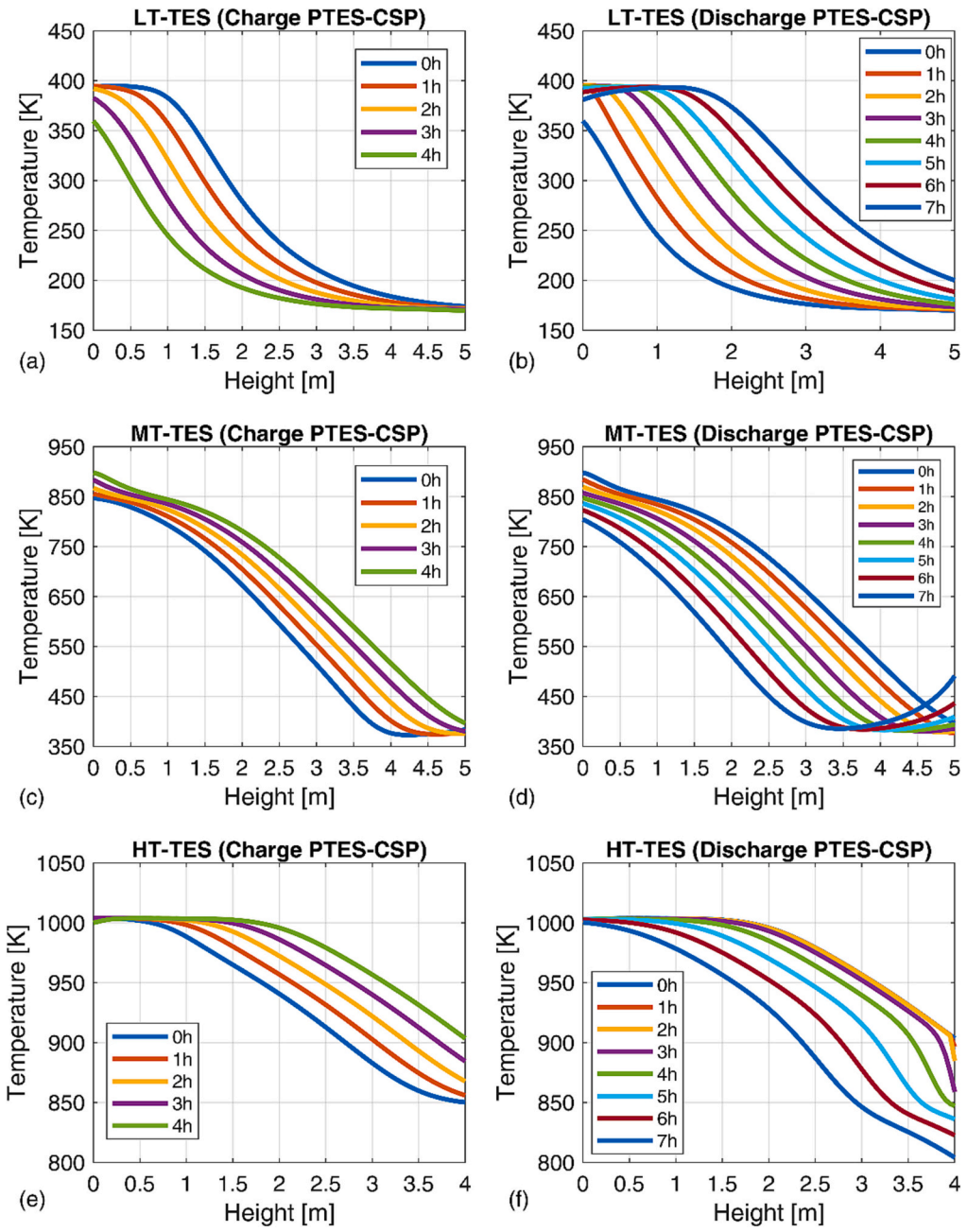

Fig. 8. Thermocline profile evolution in the three TES system during the second charging-discharging cycle for the Case A.

during the charging phase, of about 65 % for the Case A and about 63 % for the Case B are obtained.

Since the integrated plant is fed by two different energy sources (electrical energy and solar energy), an exergy roundtrip efficiency of the integrated PTES–CSP system, defined as the ratio of the electrical energy delivered during the discharging phase to the sum of the absorbed electrical energy and the exergy input in the solar receiver during the charging phase, is also evaluated, with a resulting value of about 53 % for the Case A. However, this value is influenced by the not fully discharging of the HT-TES system at the end of the day. In fact, if the exergy content in the HT-TES at the end of the day is not considered destroyed, but still available for the following day, the exergy roundtrip efficiency raises of about one point percentage (54 %). This value is confirmed by analysing the Case B when the complete discharging of all the TES is reached at the end of the second cycle. Finally, to identify the components in which the main exergy destruction occurs, Fig. 11 shows the exergy destruction rate obtained for the two test-cases. The main exergy destructions are detected in the compressors and turbines, demonstrating the relevant importance of using high-performance machines to obtain valuable roundtrip efficiencies in PTES system. On the other hand, both the machines have been designed with features representing the current state-of-the-art for the considered machines size (<10 MW) and it is hardly possible to reduce these endogenous exergy destructions. Another relevant contribution in reducing the exergy efficiency arises from the water coolers WCO2 and WCO3, due to the cooling of the working fluid at high temperature. This fact therefore suggests the implementation of appropriate changes in the plant configuration to further increase the performance of the proposed system. Marginal differences in the exergy destruction rate are detected between the two test-cases, although a yearly analysis will be required to confirm the performance obtained.

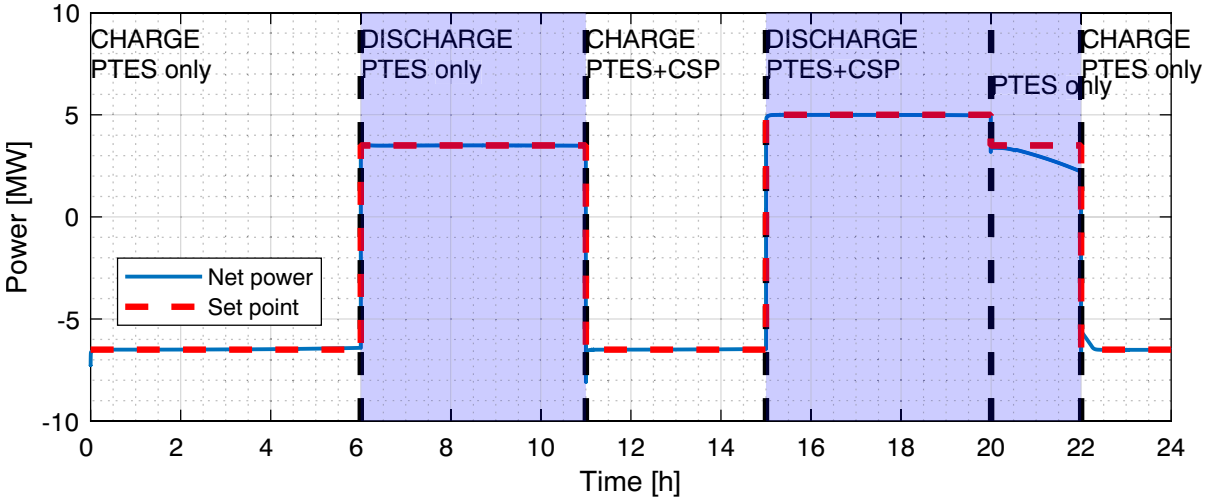

Fig. 9. Net power desired and produced by the PTES-CSP plant for the Case B.

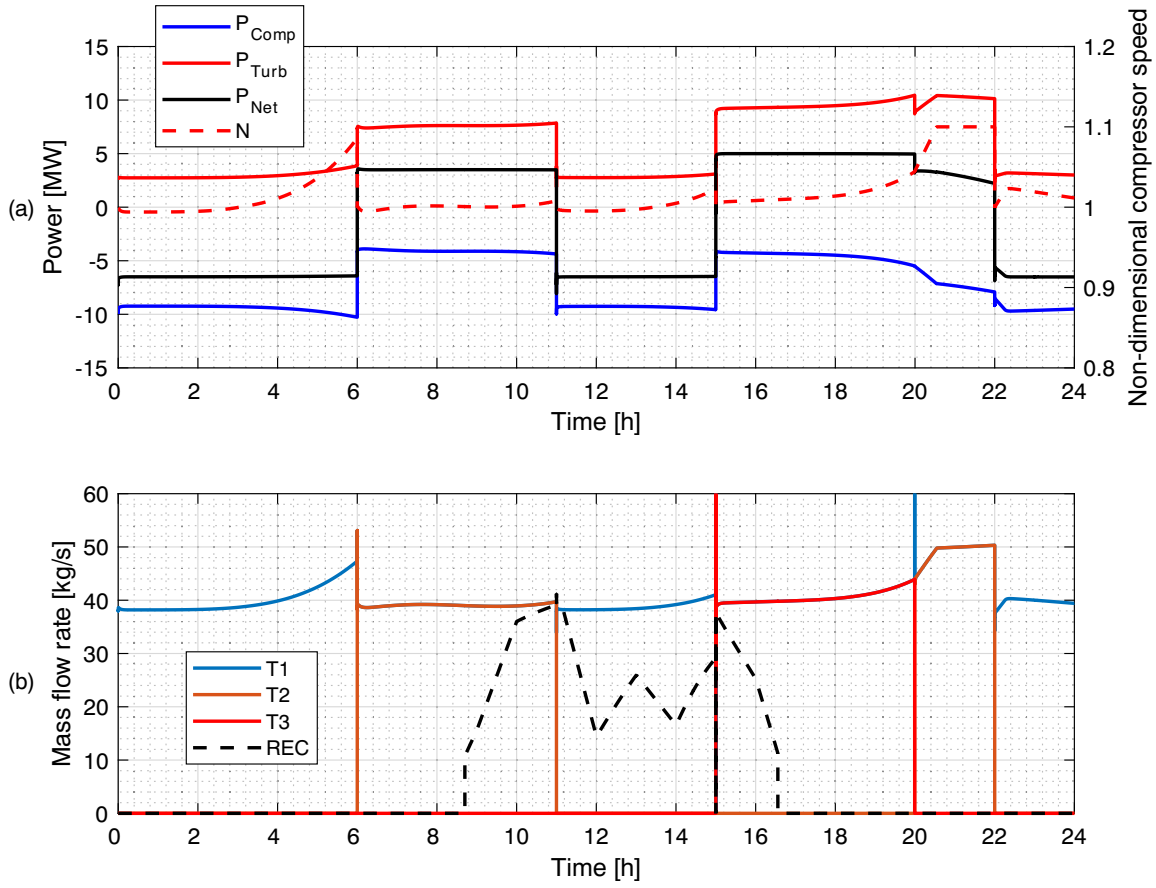

Fig. 10. (a) Compressor and turbine power curves, compressor rotational speed and (b) mass flow rates circulating in the turbines and solar receiver for the Case B.

5. Conclusions

In this paper, the expected performance of an integrated plant composed by a PTES system and a CSP plant during two different weather conditions were evaluated, by assuming the participation of the PTES subsystem in the Italian energy market for arbitrage. Starting from a given cycle configuration, the design of the main plant components was carried out and simulation models were developed to evaluate the operating performance of the overall system. An operating strategy for the energy management of the integrated plant was then proposed and implemented. The main considerations resulting from the analysis are listed below:

- The overall plant correctly follows the scheduled phases of charge and discharge, keeping the net power produced quite constant thanks to the controller system that drives the rotational speed of the compressor. The results obtained demonstrated the technical feasibility of the proposed plant configuration and the ability of the plant to follow fixed power levels. The determination of proper threshold values to be imposed for defining the fully charge/discharge state of

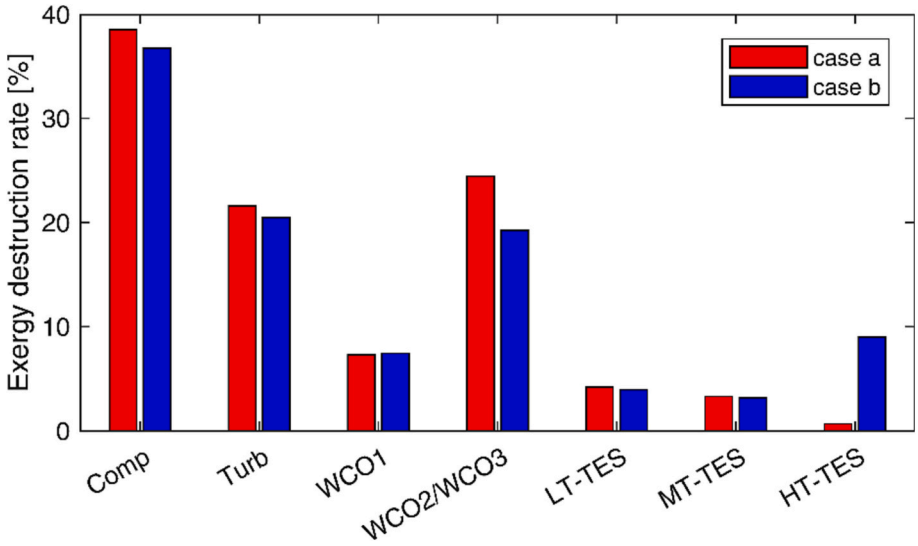

Fig. 11. Exergy destruction rate for the main components of the integrated PTES-CSP plant.

the TES is of relevant importance for a good energy management of the plant.

- The controller system has proved to be a determining factor since it allows to adequate the behavior of the compressor to keep the net power as constant as possible. In particular, the controller was able to regulate the compressor rotational speed when operative conditions at the inlet sections of both the turbines and the compressor vary.
- Suitable threshold values should be set for the terminal temperatures of the TES systems to guarantee a stable behavior of the overall plant. Numerical simulations have shown that during the discharge phase the constraints in gas temperature exiting the LT-TES system is quite decisive, since when temperature raises excessively (above 200 °C) the compressor operates close to the stall conditions making impossible for the controller to guarantee a constant net power.
- It is not easy to define a rule to set optimal threshold values for the outlet gas temperature from the TES systems, since they depend on the plant in which the TES is integrated. Preliminary simulations are decisive, to conveniently size the TES systems considering the constraints imposed to the gas temperature by the surrounding system. A good compromise was found setting a threshold of 25 K for all the TES systems, excluding the bottom value of the LT-TES that is reduced to 5 K, due to the high sensitivity of the compressor to the inlet gas temperature during the discharging phase. All these results are obtained by running five consecutive cycles, sufficient to get a TES system in a regime condition, avoiding the hysteresis phenomenon.
- The PTES system is well designed to be integrated with a CSP solar plant, with several valves included in the scheme, giving to the system a good capability to work under different DNI conditions. The solar subsystem is designed to operate with a variable mass flow rate, a requirement to keep almost constant the outlet temperature at the set-point value of 1000 K. Moreover, this component operates separately from the main management of the PTES system, since the solar subsystem can charge the HT-TES system also when the PTES system is in discharging mode.

On overall, the obtained round-trip efficiency can be considered in line with the values proposed in literature, although a slight decrease in the exergy roundtrip efficiency obtained during operating conditions (54 %) compared to the nominal one (about 58 %) was found. The determination of a similar value of exergy round trip efficiency for the two cases analysed, although characterized by a different solar availability, suggests that no large performance variations are expected during the year. However, the extension to an annual analysis of the plant performance is required for the correct evaluation of this index, which will be therefore investigated in a future work.

CRediT authorship contribution statement

Mario Cascetta: Methodology, Software, Formal analysis, Writing – original draft. **Fabio Licheri:** Conceptualization, Methodology, Software, Formal analysis, Writing – review & editing. **Rosa P. Merchán:** Methodology, Software, Formal analysis, Writing – review & editing. **Mario Petrollese:** Conceptualization, Methodology, Formal analysis, Writing – original draft.

Declaration of competing interest

The authors declare that they have no known competing financial interests or personal relationships that could have appeared to influence the work reported in this paper.

Data availability

Data will be made available on request.

References

[1] M. Jafari, A. Botterud, A. Sakti, Decarbonizing power systems: a critical review of the role of energy storage, Renew. Sust. Energ. Rev. (2022) 158, https://doi.org/10.1016/J.RSER.2022.112077.
[2] Irena, Renewable Power Generation Costs 2020, 2021.
[3] M.I. Khan, F. Asfand, S.G. Al-Ghamdi, Progress in research and technological advancements of thermal energy storage systems for concentrated solar power, J. Energy Storage 55 (2022), 105860, https://doi.org/10.1016/J.EST.2022.105860.
[4] M.M. Rahman, A.O. Oni, E. Gemechu, A. Kumar, Assessment of energy storage technologies: a review, Energy Convers. Manag. (2020) 223, https://doi.org/10.1016/J.ENCONMAN.2020.113295.
[5] A.A. Kebede, T. Kalogiannis, J. Van Mierlo, M. Berecibar, A comprehensive review of stationary energy storage devices for large scale renewable energy sources grid integration, Renew. Sust. Energ. Rev. (2022) 159, https://doi.org/10.1016/J.RSER.2022.112213.
[6] S. Pascual, P. Lisbona, L.M. Romeo, Thermal energy storage in concentrating solar power plants: a review of European and north American R&D Projects, Energies (Basel) 15 (2022) 8570, https://doi.org/10.3390/en15228570.
[7] R.P. Merchán, M.J. Santos, A. Medina, Hernández A. Calvo, High temperature central tower plants for concentrated solar power: 2021 overview, Renew. Sust. Energ. Rev. 155 (2022), 111828, https://doi.org/10.1016/j.rser.2021.111828.
[8] H. Zhang, L. Wang, X. Lin, H. Chen, Technical and economic analysis of Brayton-cycle-based pumped thermal electricity storage systems with direct and indirect

thermal energy storage, Energy (2022) 239, https://doi.org/10.1016/J.ENERGY.2021.121966.
[9] G.F. Frate, L. Paternostro, L. Ferrari, U. Desideri, Off-Design of a pumped thermal energy storage based on closed Brayton cycles, J. Eng. Gas Turbine Power (2022) 144, https://doi.org/10.1115/1.4052426.
[10] H. Yang, J. Li, Z. Ge, L. Yang, X. Du, Dynamic performance for discharging process of pumped thermal electricity storage with reversible Brayton cycle, Energy 263 (2023), 125930, https://doi.org/10.1016/J.ENERGY.2022.125930.
[11] G.F. Frate, L. Ferrari, U. Desideri, Energy storage for grid-scale applications: technology review and economic feasibility analysis, Renew. Energy 163 (2021) 1754–1772, https://doi.org/10.1016/J.RENENE.2020.10.070.
[12] Y. Zhao, J. Song, M. Liu, Y. Zhao, A.V. Olympios, P. Sapin, et al., Thermo-economic assessments of pumped-thermal electricity storage systems employing sensible heat storage materials, Renew. Energy 186 (2022) 431–456, https://doi.org/10.1016/J.RENENE.2022.01.017.
[13] A. Benato, A. Stoppato, Pumped thermal electricity storage: a technology overview, Therm. Sci. Eng. Prog. 6 (2018) 301–315, https://doi.org/10.1016/J.TSEP.2018.01.017.
[14] T.R. Davenne, B.M. Peters, An analysis of pumped thermal energy storage with decoupled thermal stores, Front. Energy Res. (2020) 8, https://doi.org/10.3389/fenrg.2020.00160.
[15] M. Albert, Z. Ma, H. Bao, A.P. Roskilly, Operation and performance of Brayton pumped thermal energy storage with additional latent storage, Appl. Energy (2022) 312, https://doi.org/10.1016/J.APENERGY.2022.118700.
[16] H. Jockenhöfer, W.D. Steinmann, D. Bauer, Detailed numerical investigation of a pumped thermal energy storage with low temperature heat integration, Energy 145 (2018) 665–676, https://doi.org/10.1016/J.ENERGY.2017.12.087.
[17] O. Dumont, G.F. Frate, A. Pillai, S. Lecompte, De paepe M, Lemort V., Carnot battery technology: a state-of-the-art review, J. Energy Storage (2020) 32, https://doi.org/10.1016/j.est.2020.101756.
[18] A. Vecchi, K. Knobloch, T. Liang, H. Kildahl, A. Sciacovelli, K. Engelbrecht, et al., Carnot battery development: a review on system performance, applications and commercial state-of-the-art, J. Energy Storage 55 (2022), 105782, https://doi.org/10.1016/J.EST.2022.105782.
[19] A.V. Olympios, J.D. McTigue, P. Farres-Antunez, A. Tafone, A. Romagnoli, Y. Li, et al., Progress and prospects of thermo-mechanical energy storage-a critical review, Prog. Energy (2020) 3, https://doi.org/10.1088/2516-1083/abdbba.
[20] L. Wang, X. Lin, H. Zhang, L. Peng, X. Zhang, H. Chen, Analytic optimization of Joule–Brayton cycle-based pumped thermal electricity storage system, J. Energy Storage (2022) 47, https://doi.org/10.1016/j.est.2021.103663.
[21] W.D. Steinmann, H. Jockenhöfer, D. Bauer, Thermodynamic analysis of high-temperature Carnot battery concepts, Energy Technol. (2020) 8, https://doi.org/10.1002/ENTE.201900895.
[22] W.D. Steinmann, D. Bauer, H. Jockenhöfer, M. Johnson, Pumped thermal energy storage (PTES) as smart sector-coupling technology for heat and electricity, Energy 183 (2019) 185–190, https://doi.org/10.1016/J.ENERGY.2019.06.058.
[23] J. Howes, Concept and development of a pumped heat electricity storage device, in: Proceedings of the IEEE vol. 100, Institute of Electrical and Electronics Engineers Inc, 2012, pp. 493–503, https://doi.org/10.1109/JPROC.2011.2174529.
[24] R.B. Laughlin, Pumped thermal grid storage with heat exchange, J. Renewable Sustainable Energy (2017) 9, https://doi.org/10.1063/1.4994054.
[25] J.D. McTigue, P. Farres-Antunez, J. KS, C.N. Markides, A.J. White, Techno-economic analysis of recuperated Joule-Brayton pumped thermal energy storage, Energy Convers. Manag. (2022) 252, https://doi.org/10.1016/J.ENCONMAN.2021.115016.
[26] T. Esence, A. Bruch, J.F. Fourmigué, B. Stutz, A versatile one-dimensional numerical model for packed-bed heat storage systems, Renew. Energy 133 (2019) 190–204, https://doi.org/10.1016/j.renene.2018.10.012.
[27] J. González-Ayala, D. Salomone-González, A. Medina, J.M.M. Roco, P.L. Curto-Risso, Hernández A. Calvo, Multicriteria optimization of Brayton-like pumped thermal electricity storage with liquid media, J. Energy Storage (2021) 44, https://doi.org/10.1016/j.est.2021.103242.
[28] H. Zhang, L. Wang, X. Lin, H. Chen, Parametric optimisation and thermo-economic analysis of Joule–Brayton cycle-based pumped thermal electricity storage system under various charging–discharging periods, Energy 263 (2023), 125908, https://doi.org/10.1016/J.ENERGY.2022.125908.
[29] H. Yang, J. Li, Z. Ge, L. Yang, X. Du, Dynamic characteristics and control strategy of pumped thermal electricity storage with reversible Brayton cycle, Renew. Energy 198 (2022) 1341–1353, https://doi.org/10.1016/J.RENENE.2022.08.129.
[30] X.J. Xue, C.Y. Zhao, Transient behavior and thermodynamic analysis of Brayton-like pumped-thermal electricity storage based on packed-bed latent heat/cold stores, Appl. Energy 329 (2023), 120274, https://doi.org/10.1016/J.APENERGY.2022.120274.
[31] E. Bellos, C. Tzivanidis, Z. Said, Investigation and optimization of a solar-assisted pumped thermal energy storage system with flat plate collectors, Energy Convers. Manag. (2021) 237, https://doi.org/10.1016/J.ENCONMAN.2021.114137.
[32] G.F. Frate, A. Baccioli, L. Bernardini, L. Ferrari, Assessment of the off-design performance of a solar thermally-integrated pumped-thermal energy storage, Renew. Energy 201 (2022) 636–650, https://doi.org/10.1016/J.RENENE.2022.10.097.
[33] J. McTigue, P. Farres-Antunez, K. Ellingwood, T. Neises, A. White, T.N. Gov, Pumped thermal electricity storage with supercritical CO 2 cycles and solar heat input, AIP Conf. Proc. 2303 (2020), 190024, https://doi.org/10.1063/5.0032337.
[34] S. Hu, Z. Yang, J. Li, Y. Duan, Thermo-economic analysis of the pumped thermal energy storage with thermal integration in different application scenarios, Energy Convers. Manag. (2021) 236, https://doi.org/10.1016/J.ENCONMAN.2021.114072.
[35] M. Petrollese, M. Cascetta, V. Tola, D. Cocco, G. Cau, Pumped thermal energy storage systems integrated with a concentrating solar power section: conceptual design and performance evaluation, Energy (2022) 247, https://doi.org/10.1016/j.energy.2022.123516.
[36] M. Casey, C. Robinson, A Method to Estimate the Performance Map of a Centrifugal Compressor Stage Background to the Method 135, 2013, pp. 21034–21035, https://doi.org/10.1115/1.4006590.
[37] W. Al-Busaidi, P. Pilidis, A new method for reliable performance prediction of multi-stage industrial centrifugal compressors based on stage stacking technique: part I - existing models evaluation, Appl. Therm. Eng. 98 (2016) 10–28, https://doi.org/10.1016/J.APPLTHERMALENG.2015.11.115.
[38] D. Rusch, M. Casey, The Design Space Boundaries for High Flow Capacity Centrifugal Compressors, 2013, https://doi.org/10.1115/1.4007548.
[39] O. Achkari, A. El Fadar, Latest developments on TES and CSP technologies – energy and environmental issues, applications and research trends, Appl. Therm. Eng. (2020) 167, https://doi.org/10.1016/J.APPLTHERMALENG.2019.114806.
[40] B. Belgasim, Y. Aldali, M.J.R. Abdunnabi, G. Hashem, K. Hossin, The potential of concentrating solar power (CSP) for electricity generation in Libya, Renew. Sust. Energ. Rev. 90 (2018) 1–15, https://doi.org/10.1016/J.RSER.2018.03.045.
[41] K. Kusterer, R. Braun, N. Moritz, T. Sugimoto, K. Tanimura, D. Bohn, Comparative study of solar thermal Brayton cycles operated with helium or argon, Proc. ASME Turbo Expo (2013) 4, https://doi.org/10.1115/GT2013-94990.
[42] H. Cherif, A. Ghomrassi, J. Sghaier, H. Mhiri, P. Bournot, A receiver geometrical details effect on a solar parabolic dish collector performance, Energy Rep. 5 (2019) 882–897, https://doi.org/10.1016/J.EGYR.2019.07.010.
[43] M. Wang, K. Siddiqui, The impact of geometrical parameters on the thermal performance of a solar receiver of dish-type concentrated solar energy system, Renew. Energy 35 (2010) 2501–2513, https://doi.org/10.1016/J.RENENE.2010.03.021.
[44] R.P. Merchán, M.J. Santos, A. Medina, A.C. Hernández, On- and off-design thermodynamic analysis of a hybrid polar solar thermal tower power plant, Int. J. Energy Res. 45 (2021) 1789–1805, https://doi.org/10.1002/er.5854.
[45] R.P. Merchán, M.J. Santos, J. García-Ferrero, A. Medina, A.C. Hernández, Thermo-economic and sensitivity analysis of a central tower hybrid Brayton solar power plant, Appl. Therm. Eng. (2021) 186, https://doi.org/10.1016/J.APPLTHERMALENG.2020.116454.
[46] I.H. Bell, J. Wronski, S. Quoilin, V. Lemort, Pure and Pseudo-pure Fluid Thermophysical Property Evaluation and the Open-Source Thermophysical Property Library CoolProp, 2014, https://doi.org/10.1021/ie4033999.
[47] Welcome to CoolProp — CoolProp 6.4.1 documentation n.d. http://www.coolprop.org/ (accessed December 14, 2022).
[48] G. Zanganeh, A. Pedretti, S. Zavattoni, M. Barbato, A. Steinfeld, Packed-bed thermal storage for concentrated solar power - pilot-scale demonstration and industrial-scale design, Sol. Energy 86 (2012) 3084–3098, https://doi.org/10.1016/j.solener.2012.07.019.
[49] L. Chai, J. Liu, L. Wang, L. Yue, L. Yang, Y. Sheng, et al., Cryogenic energy storage characteristics of a packed bed at different pressures, Appl. Therm. Eng. 63 (2014) 439–446, https://doi.org/10.1016/J.APPLTHERMALENG.2013.11.030.
[50] F.E. Heuze, High-temperature mechanical, physical and thermal properties of granitic rocks— a review, Int. J. Rock Mech. Min. Sci. Geomech. Abstr. 20 (1983) 3–10, https://doi.org/10.1016/0148-9062(83)91609-1.
[51] M. Cascetta, F. Serra, S. Arena, E. Casti, G. Cau, P. Puddu, Experimental and numerical research activity on a packed bed TES system, Energies (Basel) 9 (2016) 758, https://doi.org/10.3390/en9090758.
[52] N. Wakao, S. Kaguei, Heat and Mass Transfer in Packed Beds. New York, 1982.
[53] D. Kunii, J.M. Smith, Heat transfer characteristics of porous rocks, AICHE J. 6 (1960) 71–78, https://doi.org/10.1002/AIC.690060115.
[54] M. Amelio, P. Beraldi, V. Ferraro, M. Scornaienchi, F. Rovense, Optimization of heliostat field in a thermal solar power plant with an unfired closed Joule-Brayton cycle, Energy Procedia 101 (2016) 472–479, https://doi.org/10.1016/J.EGYPRO.2016.11.060.
[55] S.M. Flueckiger, B.D. Iverson, S.V. Garimella, J.E. Pacheco, System-level simulation of a solar power tower plant with thermocline thermal energy storage, Appl. Energy 113 (2014) 86–96, https://doi.org/10.1016/J.APENERGY.2013.07.004.
[56] F. Rovense, M. Amelio, V. Ferraro, N.M. Scornaienchi, Analysis of a concentrating solar power tower operating with a closed joule Brayton cycle and thermal storage, Int. J. Heat Technol. 34 (2016) 485–490, https://doi.org/10.18280/IJHT.340319.
[57] S. Kakaç, H. Liu, A. Pramuanjaroenkij, Heat Exchangers: Selection, Rating, and Thermal Design, 3rd edition, CRC Press, 2012.
[58] F. Casella, E. Casati, P. Colonna, Optimal operation of solar tower plants with thermal storage for system design, IFAC Proc. Vol. 47 (2014) 4972–4978, https://doi.org/10.3182/20140824-6-ZA-1003.02622.
[59] C. Wang, S. Guo, H. Pei, Y. He, D. Liu, M. Li, Rolling optimization based on holism for the operation strategy of solar tower power plant, Appl. Energy 331 (2023), 120473, https://doi.org/10.1016/j.apenergy.2022.120473.